PHYSICAL REVIEW E **80**, 036308 (2009)

Steady-state, simultaneous two-phase flow in porous media: An experimental study

Ken Tore Tallakstad,[1,*] Grunde Løvoll,[1] Henning Arendt Knudsen,[1] Thomas Ramstad,[2,3]
Eirik Grude Flekkøy,[1] and Knut Jørgen Måløy[1]
[1]*Department of Physics, University of Oslo, PB 1048 Blindern, NO-0316 Oslo, Norway*
[2]*Department of Physics, Norwegian University of Science and Technology, NO-7491 Trondheim, Norway*
[3]*Numerical Rocks AS, Stiklestadveien 1, NO-7041 Trondheim, Norway*
(Received 16 April 2009; published 15 September 2009)

We report on experimental studies of steady-state two-phase flow in a quasi-two-dimensional porous medium. The wetting and the nonwetting phases are injected simultaneously from alternating inlet points into a Hele-Shaw cell containing one layer of randomly distributed glass beads, initially saturated with wetting fluid. The high viscous wetting phase and the low viscous nonwetting phase give a low viscosity ratio $M=10^{-4}$. Transient behavior of this system is observed in time and space. However, we find that at a certain distance behind the initial front a "local" *steady-state* develops, sharing the same properties as the later "global" steady state. In this state the nonwetting phase is fragmented into clusters, whose size distribution is shown to obey a scaling law, and the cutoff cluster size is found to be inversely proportional to the capillary number. The steady state is dominated by bubble dynamics, and we measure a power-law relationship between the pressure gradient and the capillary number. In fact, we demonstrate that there is a characteristic length scale in the system, depending on the capillary number through the pressure gradient that controls the steady-state dynamics.

DOI: 10.1103/PhysRevE.80.036308 PACS number(s): 47.56.+r, 47.55.dd, 47.55.Ca, 89.75.Fb

I. INTRODUCTION

There is truly a broad range of different immiscible multiphase flows in porous media [1–3]. Intrigued by the observed complex dynamics and geometry, researchers have over the past decades taken great interest to explain and model these systems [1–7]. Not only is it important to understand these processes from a scientific point of view, but there are also huge commercial advantages. Many questions in this field still remain unanswered; thus, to develop a better understanding is highly warranted.

Traditionally, experimental and theoretical works focused on invasion processes: pure drainage (a nonwetting fluid displacing a wetting fluid from a porous medium), or pure imbibition (a wetting fluid displacing a nonwetting fluid from a porous medium) [8,9]. Different displacement patterns were observed and classified into capillary fingering [6,10], which has been modeled by invasion percolation [11], viscous fingering [7,12–16], and stable front displacement [8,17,18]. Later experimental work has also been done by Tsakiroglou *et al.*, focusing on transport coefficients of such systems [19–22]. The common feature of these effects is that they are inherently transient. In large-scale reservoir systems there will be regions and length scales where one or both of the fluids are fragmented and transported as bubbles, i.e. dynamically very different from the regimes described above. This transport is governed by the interplay and competition between drainage and imbibition, and it is not sufficient to look at these two processes separately. We therefore approach this problem by studying the steady-state regime experimentally on laboratory scale inside "a representative elementary volume."

This kind of flow regime, where drainage and imbibition are occurring simultaneously, has received less attention than the now classic "pure invasion" problems. There is a short literature listing of steady-state pore-scale studies, but to the best of our knowledge little experimental data are available. Avraam and Payatakes [23–25] did pore-scale steady-state experiments using etched two-dimensional glass models. Their main focus was relative permeability and a qualitative description and classification of flow regimes. Payatakes and co-workers worked on numerical modeling and theory for such problems [26–30]. In an experimental setup quite similar to ours, Vedvik *et al.* did experiments on fragmentation of capillary fingering clusters in a background viscous field [31]. Also numerical work has focused on a steady-state regime. By means of two-dimensional numerical network simulations Knudsen *et al.* and Ramstad and Hansen studied average flow properties and cluster formation in steady-state two-phase flow [32–35].

In this paper we report on an experiment, in which a nonwetting fluid with low viscosity (air) and a highly viscous wetting fluid (a glycerin/water solution) simultaneously are injected into a horizontal two-dimensional porous medium. Hence, gravity has no influence on the displacement. The medium is initially saturated with the wetting fluid, and we investigate the initial transient regime, where the two fluids mix, invade, and fill the system. We demonstrate that a steady state is reached after some characteristic time. By letting the injection continue beyond this point, we study the flow dynamics and transport properties in steady state. The main characteristic of this process is that the nonwetting fluid is broken up and transported through the system as disconnecting bubbles. We therefore pay special attention to the size distribution of nonwetting clusters (bubbles). For six different injection rates (spanning a range of two orders of magnitude), the probability density of cluster size is measured and found to obey a scaling law. We also report results

---

[*] k.t.tallakstad@fys.uio.no

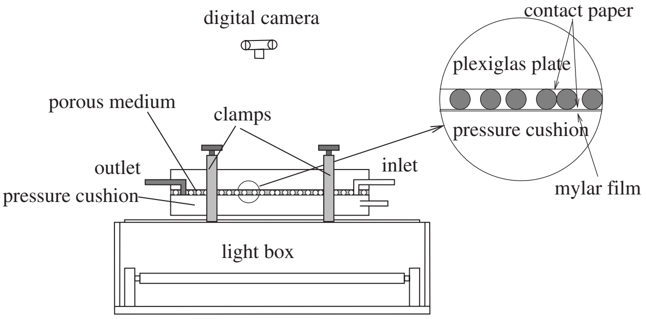

FIG. 1. Sketch of the experimental setup with the light box for illumination, the porous model, and the digital camera. The porous medium is sandwiched between two contact papers and kept together and temperature controlled with a water-filled pressure cushion.

on the relation between the global pressure, a characteristic cluster length scale, and the capillary number.

II. EXPERIMENTAL SETUP

The experimental setup is shown in Figs. 1 and 2. We use a monolayered porous stratum consisting of glass beads of diameter $a=1$ mm, randomly spread between two contact papers [16,17]. The model is a transparent rectangular box of dimensions $L\times W=850\times 420$ mm^2 and thickness a (see Table I for a listing of model parameters).

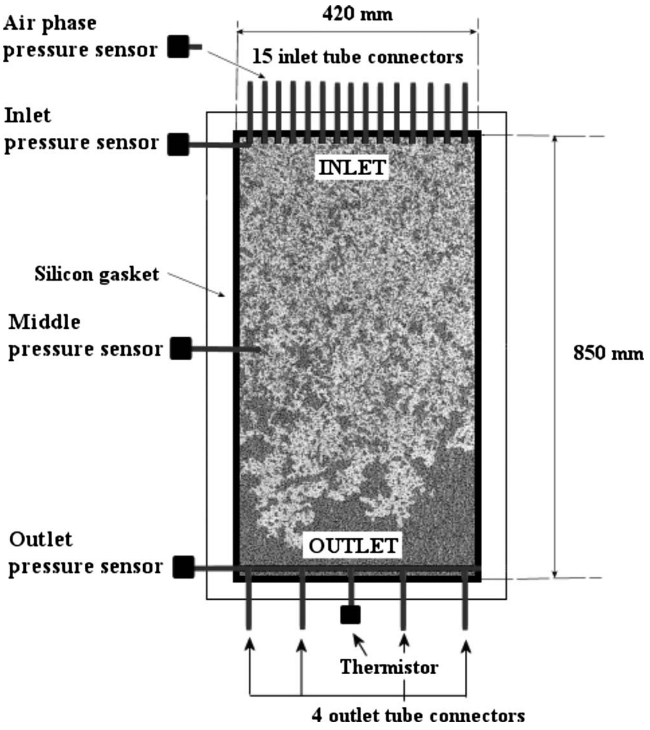

FIG. 2. Sketch of the experimental model. There are 15 independent inlet holes with attached tubes where we inject (alternately) the wetting and the nonwetting phase with syringe pumps. This leads to a mixing of the two phases inside the model two-dimensional porous medium (a random monolayer of glass beads) and a mix of the two phases flows out of the outlet channel at the opposite end of the system. In one of the inlet tubes (nonwetting phase) and in the porous model (wetting phase) pressure sensors are mounted for pressure measurements.

TABLE I. Geometrical parameters of the experimental setup and measured fluid properties. The absolute permeability κ_0 is measured in a separate experiment with the wetting fluid only.

Description	Symbol	Value
Model length	L	850 mm
Model width	W	420 mm
Bead diameter	a	1.0 mm
Porosity	ϕ_0	0.63
Permeability	κ_0	$(1.95\pm 0.1)\times 10^{-5}$ cm^2
Wetting fluid viscosity	μ_w	0.11 Pa s
Nonwetting fluid viscosity	μ_{nw}	1.9×10^{-5} Pa s
Wetting fluid density	ρ_w	1217 kg m^{-3}
Nonwetting fluid density	ρ_{nw}	1.168 kg m^{-3}
Viscosity ratio	M	$\sim 10^{-4}$
Surface tension	γ	6.4×10^{-2} N m^{-1}

A 2-cm-thick Plexiglas plate is placed on top of the model. In order to squeeze the beads and the contact paper together with the upper plate, a Mylar membrane mounted on a 2.5-cm-thick Plexiglas plate, below the model, is kept under a 3.5 m water pressure as a "pressure cushion." The upper and the lower plates are kept together by clamps, and the side boundaries are sealed by a rectangular silicon rubber packing. The upper plate has 15 independent drilled inlets for fluid injection and a milled outlet channel (Fig. 2). The distance between the inlets and the outlet channel defines the length of the model.

The wetting fluid used in all our experiments is a 85−15 % by weight *glycerol-water* solution dyed with 0.1% Negrosine (black color). *Air* is used as the nonwetting fluid. This gives a black and white fluid pair with good visual contrast. The wetting and the nonwetting fluids have viscosities of $\mu_w\approx 0.11$ Pa s and $\mu_{nw}=1.9\times 10^{-5}$ Pa s, respectively. The viscous ratio is thus $M=\mu_{nw}/\mu_w\sim 10^{-4}$, which is typical for a gas/liquid system. Other fluid parameters are found in Table I. The model is held at a constant temperature of 20 °C during the experiments. This is monitored by measuring the temperature in the wetting fluid at the outlet, thus allowing an accurate estimation of the viscosity of the fluid.

During experiments the pressure is recorded at four different positions, in one of the air inlet tubes and in the wetting fluid at the edge of the model: close to the inlet, at a distance $L/2$ in the flow direction, and in the outlet channel (Fig. 2) using SensorTechnics 26PC0100G6G Flow Through pressure sensors.

The flow structure is visualized by illuminating the model from below with a light box and pictures are taken at regular intervals with a Pixelink Industrial Vision PL-A781 digital camera, which is controlled by a computer over a FireWire connection. This computer records both the pictures and the pressure measurements. Each image contains 3000×2208 pixels, which corresponds to a spatial resolution of ~ 0.19 mm per pixel (27 pixels in a pore of size of 1 mm^2).

The color scale contains 256 gray levels. The gray level distribution of the image presents two peaks corresponding, respectively, to the white air-filled and dark gray glycerol-filled parts of the image. The image is thresholded at a constant offset from the white peak so as to obtain a representative boundary between the two phases [18]. All further image treatments are performed on the resulting black and white image. The exact choice of the threshold value influences the extracted results. However, by visual inspection and analyses of results from a range of threshold values around the chosen one, the deviations are found to be small and systematic with this perturbation. We therefore claim that this procedure of choosing the threshold value is consistent and that the resulting data may be compared directly.

Close to the inlet and to a small degree along the model perimeter, there are boundary effects in the displacement structure. To avoid these, we define a (69×30) cm region of interest (ROI) in the central part of the model. Image analysis is then performed only inside this ROI.

In all experiments the porous model is initially filled with the wetting glycerol-water solution. An experiment is then started by injecting the wetting fluid and the nonwetting fluid from every other inlet hole (Fig. 2). Counting from one side this means that syringes $1,3,5,\ldots,15$ altogether eight individual syringes for the wetting fluid are used for the injection. Similarly, syringes $2,4,6,\ldots,14$ altogether seven individual syringes are used for the nonwetting fluid. The movements of all 15 syringes are controlled by the same step motor, setting an equal displacement rate.

III. RESULTS

As the nonwetting fluid enters the model, it first forms elongated clusters which are connected with their respective inlets. As these clusters grow, they are snapped off by the wetting fluid and transported as bubbles along the flow toward the outlet of the model. Over time the nonwetting air clusters propagate all the way to the outlet of the model, thus filling the whole porous matrix with a mixture of air and glycerol-water solution. The air only exists in the form of fragmented clusters while the glycerol-water solution percolates the model at all times. It is observed that the smallest air clusters usually are immobile and trapped. Larger clusters on the other hand are mobile and propagate in the porous medium. However, mobilization of trapped clusters can occur when they coalesce with larger migrating clusters. Conversely, fragmentation and trapping of migrating clusters also take place, so the fate of an air cluster is thus highly undecided. In this context it is worth mentioning the detailed pore-scale study of cluster mobilization and entrapment by Avraam and Payatakes [23,39].

We run the experiment for a significant time after air breakthrough. Shortly after breakthrough the transport process reaches steady state, meaning that both phases are transported through the model without "long-time" flow parameter changes, implying that the pressure difference, relative permeabilities, saturations, and cluster distributions are on average constant. Images of the evolution of the transient part of a typical experiment are shown in Fig. 3.

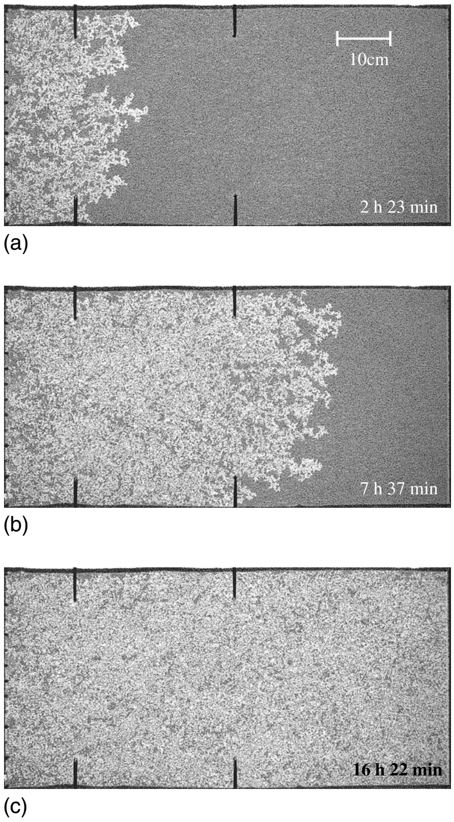

FIG. 3. For the Ca=0.0079 experiment, the system is shown at three different times. Both fluids are injected at left hand side; the outlet is at the right. The upper panel shows a sample in the early transient regime. The water-glycerol mixture is of dark color. This is best seen to the right of the upper panel, where the small bright dots are the solid glass beads. The air is bright white, and glass beads surrounded by air may be indiscernible. The middle panel shows a later stage in the transient. The lower panel shows fully developed steady state.

In Fig. 4 pressure differences over the model are plotted as function of time. Three pressure sensors are used: at the inlet, in the middle of the model, and at the outlet. Even though pressure measurements are local, and measured in the wetting phase, they reflect on average the global pressure development of both phases. If both phases are present along a given cross section transverse to the flow, the pressure along this cross section will only vary by small capillary and viscous fluctuations. Due to the size of our system and the high viscosity of the wetting phase, the measured pressure drop is much larger than these fluctuations. Physically relevant for the motion inside the model is the pressure difference between (i) inlet and outlet and (ii) middle of the model and outlet which, for brevity, are referred to as *inlet* and *middle pressures*. In Fig. 4(a) we can see the signature of a "breakthrough" just before $t\simeq 60$ min in the pressure signals. Here, the apparent linear increase in pressure stops. Shortly after this time the two signals approach a constant level as we reach steady state. In the transient regime the overall pressure behavior at the two sensors appears different. As air enters the model, the inlet pressure starts to increase and it increases linearly until breakthrough, while the

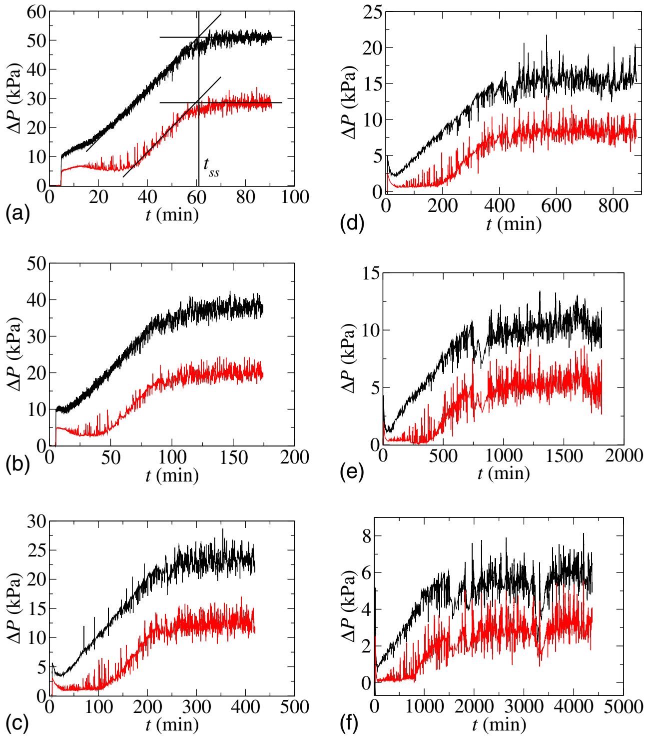

FIG. 4. (Color online) Time evolution of the pressure in each of the six experiments, performed at different injection rate, which is denoted in terms of the capillary numbers (a) Ca=0.17, (b) Ca =0.90, (c) Ca=0.032, (d) Ca=0.015, (e) , and (f) Ca=0.027. The upper black curves are the measured pressure differences between the inlet and the outlet. The lower red (dark gray) curves are the pressure differences between the middle of the model and the outlet. The straight line fit to the pressure curves in (a) shows the determination of the steady-state time t_{ss}, i.e., at which time the system enters into steady state.

middle pressure is constant until the air bubbles reach the sensor (~30 min). At this point the middle sensor pressure also starts to increase linearly. This is because the average pressure at a point inside the porous medium is controlled by the viscous pressure drop between that point and the outlet channel. Moreover, as air bubbles pass the sensor, the effective permeability of the medium in front of the sensor is lowered. In order to maintain constant flow rate, the pressure has to increase.

In order to learn more about the transient and the transition to steady state, here, we present the results of six experiments performed at different injection rates. The injection rate is controlled by the speed of the step motor used to control the syringe pistons. The rates and the corresponding capillary numbers are given in Table II. We define the capillary number as the ratio between the viscous and the capillary pressure drops over a pore of typical size a,

$$\mathrm{Ca} = \frac{\mu_w Q_w a^2}{\gamma \kappa_0 A} = \frac{\mu_w a^2 v_w}{\gamma \kappa_0}, \tag{1}$$

where $A = Wa$ is the cross-sectional area, $Q_w = 8Q_0$ is total flow rate of the wetting fluid, and v_w is the Darcy velocity of the wetting fluid.

TABLE II. For each of six experiments are given the capillary number, the corresponding flow rate out of a single syringe pump Q_0, the total flow rate $15Q_0$, and the "total invasion flow rate" Q_{tot}^{inv} (see Fig. 14). The difference between $15Q_0$ and Q_{tot}^{inv} is due to compressibility effects as will be discussed in Sec. III D. The capillary number is calculated from Eq. (1).

Ca	Q_0 (ml/min)	$15Q_0$ (ml/min)	Q_{tot}^{inv} (ml/min)
0.17	0.553	8.29	5.73
0.090	0.279	4.18	2.90
0.032	0.114	1.71	1.29
0.015	0.055	0.83	0.67
0.0079	0.023	0.41	0.35
0.0027	0.011	0.16	0.15

A. Transient behavior

A first characteristic time in the transient regime is the elapsed time from onset of invasion until the first breakthrough of nonwetting fluid (air). Recall that the model initially is filled with wetting fluid. We determine this breakthrough time t_b by visual inspection in each experiment. A second characteristic time is when all signs of transient behavior vanish: the steady-state time t_{ss}. To some degree it is possible to see the transition to steady state also by visual inspection. However, as opposed to the breakthrough time, which is sharply defined visually, the steady-state time is not so sharply defined in this way.

In order to quantize the steady-state time, we make use of the measured pressure curves. Figure 4 shows the evolution of the pressure difference between (i) inlet and outlet and (ii) middle point and outlet for each experiment. The pressure saturates and fluctuates around some value at late times in all cases. Prior to saturation there is a period of close to linear increase in the pressure. By making a straight line fit to this slope and flat line fit to the saturated value, we define their crossing point to be the steady-state time t_{ss}, as shown in Fig. 4(a). This definition is sharp and consistent in the sense that this time is the same no matter which of the pressure measurement points (inlet or middle) is used.

The resulting characteristic times versus the capillary number are plotted in Fig. 5. Power-law fits are obtained as shown in the legend. Leaving out details of the process one

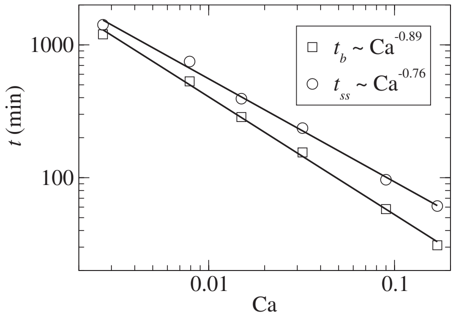

FIG. 5. Measured breakthrough time t_b and steady-state time t_{ss} as a function of the capillary number Ca.

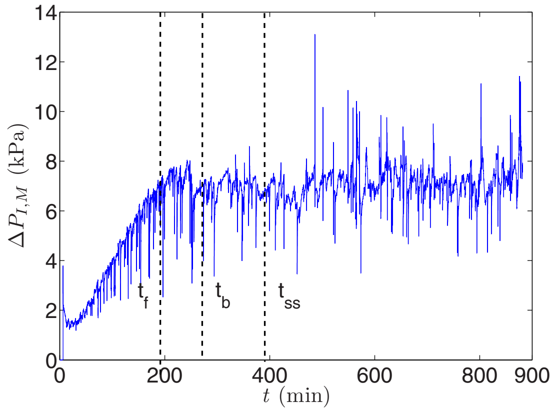

FIG. 6. (Color online) Pressure difference between inlet and middle sensor $\Delta P_{I,M}$ as a function of time t for Ca=0.015. Three characteristic times are indicated by dashed lines; the time at which the front passes the middle sensor t_f, the breakthrough time t_b, and steady-state time t_{ss}.

would expect these times to be proportional to the inverse injection rate. The deviations in the found exponents are small, but nevertheless indicating that there are variations in invasion structure and saturation with Ca.

B. Steady state

In Sec. III A we learned that there exists a well-defined transition to steady state based on analysis of the pressure signal. This is a global criterion, meaning that the system as a whole has reached a steady state. We wish to look at this also on a local scale.

From the onset of invasion a frontal region establishes, containing quite large nonwetting clusters (see Fig. 3). Here, the wetting saturation is somewhat larger than compared to the region behind the frontal region. In addition the region behind the front is more fragmented and homogeneous. We claim that, locally, the region behind the front has already entered into steady state. This is interesting because this happens very early in the process. The region with local steady state grows as the front sweeps through the model. Two arguments support this observation.

First, there is the fact that the pressure monitored by the middle sensor increases linearly from a time t_f right after the front has reached the sensor [see Fig. 4(d)]. This linear increase has the same slope as the inlet sensor pressure until steady state is reached globally (see Fig. 6). For all experiments we find that the pressure difference between the inlet and the middle sensors, $\Delta P_{I,M}(t_f<t<t_{ss})$, during this linear increase is hardly distinguishable from $\Delta P_{I,M}(t>t_{ss})$, as shown in Fig. 6. Since the displacement rate is constant and close to equal both in the transient and the steady states, it follows from Fig. 6 that the relative permeability of the region behind the front must equal that of the later global steady state.

Second, image analyses of parts of the model behind the front in the transient regime as well as in global steady state were performed, yielding similar results for saturation and cluster distribution. This statistical equality and the above results demonstrate that the region behind the front is in local steady state.

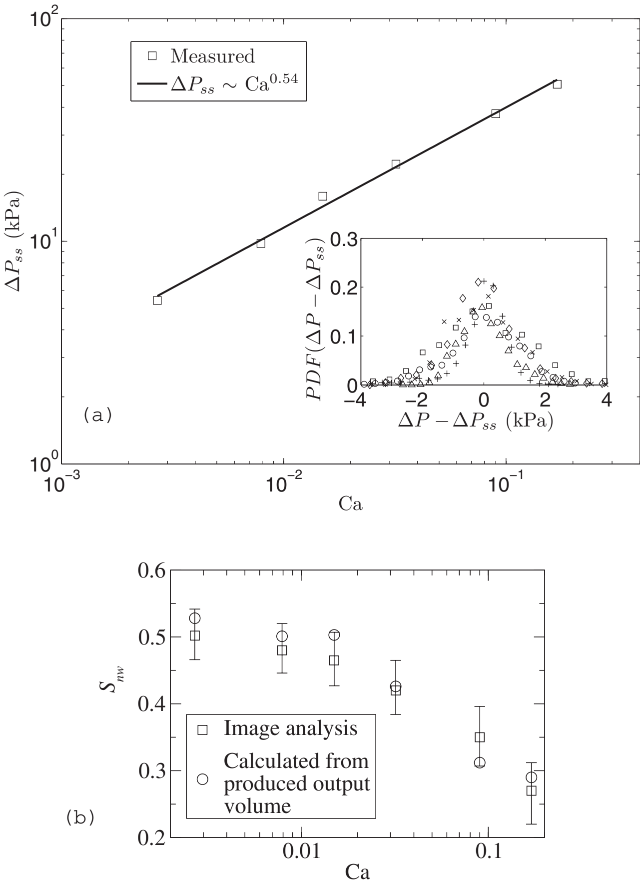

FIG. 7. (a) Average steady-state pressure difference ΔP_{ss} vs capillary number Ca. The solid line is a power-law fit to the measured points giving an exponent β=0.54±0.08. Inset shows the Gaussian-like PDF of $\Delta P(t>t_{ss})-\Delta P_{ss}$. Note that for all experiments the fluctuations are small and on the order of 1 kPa. (b) The nonwetting saturation S_{nw} as a function of the capillary number Ca.

The global steady state can be quantized by the averaged global pressure drop between the inlet and the outlet,

$$\Delta P_{ss} = \frac{1}{t_{end}-t_{ss}}\int_{t_{ss}}^{t_{end}} \Delta P(t)dt, \tag{2}$$

where t_{end} is the end time of the experiment and the nonwetting fluid saturation S_{nw} [see Figs. 7(a) and 7(b)].

Experimentally, saturation is not an easily accessible parameter and two approaches have been employed to determine the saturation [see Fig. 7(b)]. A direct method uses the measured amount of wetting fluid that leaves and enters the model. It is in principle a precise method, but it is global. Possible boundary effects, e.g., different saturations near edges or corners, are ignored. Further, image analysis was used by setting a certain grayscale clipping level, as described in Sec. II, and then from the binary image count the amount of wetting fluid.

One observes that the nonwetting saturation decreases with increasing the total injected flow rate. The constraint that the fractional flow is kept constant, a situation for which little previous results exists, makes it difficult to say whether this is intuitively correct. Numerical studies have sought after relations between saturation and other flow properties [33,34]. However, another factor, to be discussed in Sec. III D, are possible compressibility effects. It is *a priori* not clear that the saturation would be the same if the air were incompressible. This is an issue that we will pursue in further studies.

Figure 7(a) shows the mean steady-state pressure difference ΔP_{ss} as a function of the capillary number Ca. The pressure fluctuations are small as shown in the pressure distributions PDF($\Delta P - \Delta P_{ss}$) in the inset of Fig. 7(a). For all experiments the standard deviation in ΔP_{ss} is on the order of 1 kPa. It is evident that ΔP_{ss} follows a power law in Ca,

$$\Delta P_{ss} \propto \mathrm{Ca}^{\beta}, \tag{3}$$

with the exponent

$$\beta = 0.54 \pm 0.08. \tag{4}$$

This behavior is by no means obvious [36], and we will return to a physical interpretation and quantitative derivation of this result in Sec. III C.

C. Cluster size distributions

After the systems have entered into steady state, we have analyzed images of the structure in order to determine the size distribution of nonwetting clusters or bubbles. The normalized probability density function (PDF) $p(s)$ as a function of cluster size s for all Ca numbers investigated is shown in Fig. 8(a). A trivial observation is the decrease in probability with increasing cluster size. Less obvious is the fact that the curves show an exponential-like cutoff depending on the capillary number. Additionally there is a cutoff region for smaller clusters, as the cluster size approaches the bead size. Since the beads are counted as part of the clusters during image analysis, we have no information at this size scale. For the highest Ca numbers, the whole distribution is dominated by the exponential cutoff. However, as the Ca number is decreased, a small region of power-law-like behavior is observed in between the two cutoffs.

Analogously to what is done in percolation theory [37], we assume that the distribution of the clusters follows the PDF,

$$p(s) \propto s^{-\tau} \exp(-s/s^*), \tag{5}$$

where s^* is the cutoff cluster size. The latter function has been fitted, using a proportionality constant τ and s^* as fit parameters, to the experimental data for each Ca number. This is shown by the solid lines in Fig. 8(a). By averaging the fitted τ exponents it is found that $\tau = 2.07 \pm 0.18$. The uncertainty only reflects the difference in fitted exponents. From the distributions it is seen that no power-law region is well pronounced, and we do not claim that τ is determined with a large degree of certainty in this case. When it comes to the cutoff cluster size, the fitted values of s^* are found to scale with Ca [Eq. (1)] as

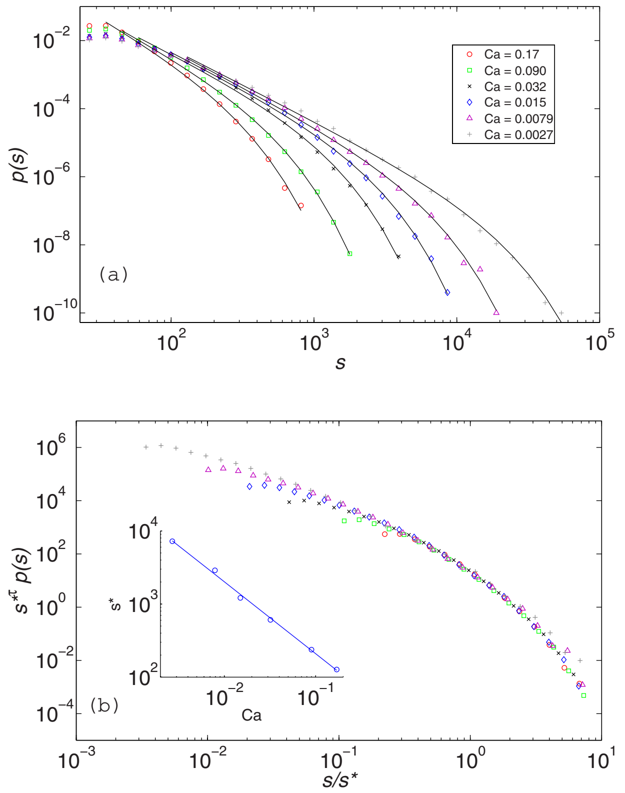

FIG. 8. (Color online) Nonwetting cluster size PDF $p(s)$ in steady state for all experiments. The cluster size s is measured in pixels; 1 pixel=0.037 mm^2. (a) Normalized probability distributions. The dominating cutoff behavior is evident. The solid lines represent fits of Eq. (5). (b) The horizontal and the vertical axes are rescaled with $1/s^*$ and $s^{*\tau}$, respectively, to obtain the data collapse. The Ca dependence of the cutoff cluster size s^* is shown in the inset.

$$s^* \propto \mathrm{Ca}^{-\zeta}, \tag{6}$$

where $\zeta = 0.98 \pm 0.07$. This is shown in the inset of Fig. 8(b). One should note, even for the lowest Ca number, that $s^* \sim 10^5$ pixels is considerably smaller than the system size $\sim 10^7$ pixels, meaning that large-scale finite-size effects should not be of importance. Equation (5) predicts a rescaling of the horizontal and the vertical axes with $1/s^*$ and $s^{*\tau}$, respectively. On this basis the data collapse in Fig. 8(b) is obtained.

From the above considerations, the cluster size PDF of nonwetting clusters in steady state obeys the scaling function

$$p(s) \propto s^{*-\tau} H(s/s^*), \tag{7}$$

where $H(x)$ contains an exponential cutoff [Eq. (5)], so that $p(s) \to 0$ when $x \gg 1$.

Up to now the cluster size measured in area was studied. One step further is to consider the linear extension of the clusters in the two directions: l_x transverse to the overall direction of flow and l_y oriented along the overall direction of flow. This is achieved by assigning a bounding box of sides l_x and l_y to a cluster of size s, i.e., the smallest rectangle that can contain the cluster. In the following, l_i, where $i \in \{x, y\}$, will denote both the l_x and the l_y extensions. It is

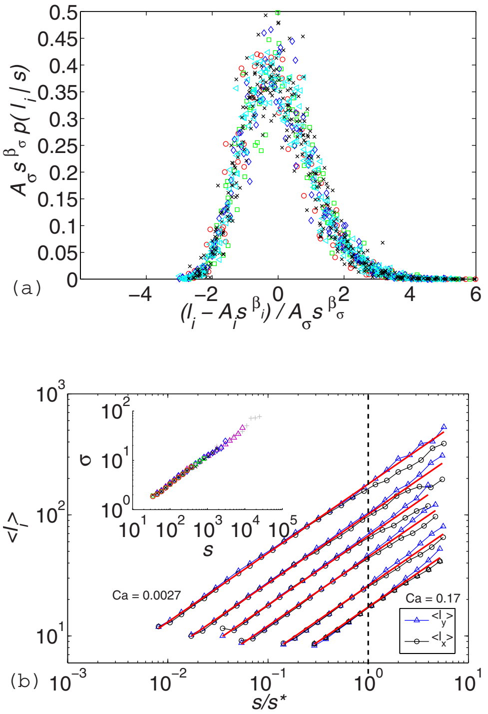

FIG. 9. (Color online) The extension lengths l_i are measured in pixel units; 1 pixel=0.19 mm. (a) Data collapse of multiple $p(l_i|s)$ PDFs, where $i \in \{x,y\}$. The s values are picked from all experiments and ranges over four decades. The collapse is obtained by a rescaling predicted by the Gaussian distribution function. (b) Scaling of $\langle l_y \rangle$ and $\langle l_x \rangle$ with s for all Ca numbers. The horizontal axis has been rescaled with $1/s^*$ to emphasize that Eq. (9), represented by the solid red (dark gray) lines, shows deviations for $s > s^*$. The inset shows the scaling of σ with s, [Eq. (8)].

found that the PDF of l_i for a given cluster size s, $p(l_i|s)$, is a Gaussian. Additionally, for $s \leq s^*$, the corresponding standard deviation σ and mean $\langle l_i \rangle$ of $p(l_i|s)$ scale with the cluster size as

$$\sigma = A_\sigma s^{\beta_\sigma}, \tag{8}$$

$$\langle l_i \rangle = A_i s^{\beta_i}, \tag{9}$$

with prefactors $A_\sigma = 0.25$ and $A_i = 1.12$, where $\beta_\sigma = 0.55 \pm 0.06$ and $\beta_i = 0.57 \pm 0.05$. Within the limits of uncertainty, β_σ and β_i can be considered equal. The corresponding prefactors yield

$$\sigma / \langle l_i \rangle \approx 0.22, \tag{10}$$

meaning that the standard deviation is roughly 22% of the mean extension length.

The collapse of multiple $p(l_i|s)$ PDFs of different cluster sizes and Ca numbers and the scaling of Eqs. (8) and (9) are shown in Figs. 9(a) and 9(b), respectively. Figure 9(a) reveals a strong correlation between cluster size and linear extension, and we believe that the use of bounding boxes to characterize the clusters is justified. It is evident from Fig. 9(b) that the scaling of $\langle l_x \rangle$ and $\langle l_y \rangle$ is equal for $s \leq s^*$, a point to which we will return shortly. However, at this stage we note that the cutoff cluster size s^* corresponds to a cutoff extension length l^*. From Eqs. (6) and (9) it follows that

$$l^* = A_i s^{*\beta_i} \propto \mathrm{Ca}^{-\zeta\beta_i}. \tag{11}$$

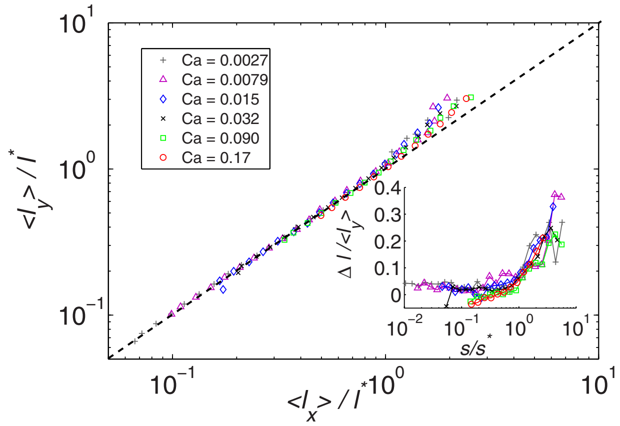

FIG. 10. (Color online) Average extension length $\langle l_x \rangle$ vs $\langle l_y \rangle$, with both axes rescaled with the cutoff length l^*. Clusters are not elongated, on the average, until l^* is reached. The inset shows the relative length difference $\Delta l / \langle l_y \rangle$ as a function of s/s^*, where $\Delta l = \langle l_y \rangle - \langle l_x \rangle$. $\Delta l / \langle l_y \rangle$ increases significantly when s^* is reached.

The similar scaling of $\langle l_i \rangle$ for $s \leq s^*$ means that nonwetting clusters fit into quadratic bounding boxes on the average and can thus be considered isotropic at these sizes. This is seen from Fig. 10 where $\langle l_x \rangle$ is plotted vs $\langle l_y \rangle$, both rescaled with the cutoff extension length l^*. It is evident that the average bounding box for $\langle l_i \rangle \leq l^*$ is quadratic, and furthermore this behavior is independent of Ca. When $\langle l_i \rangle$ reaches l^*, equivalent to the cluster size reaching s^*, there is a crossover and the clusters are seen to be somewhat elongated in the direction of flow on the average. Cluster elongation or anisotropy is best emphasized by considering the average relative length difference $\Delta l / \langle l_y \rangle$, where $\Delta l = \langle l_y \rangle - \langle l_x \rangle$. The inset of Fig. 10 shows, for six Ca numbers, the relative length difference for all cluster sizes. Each curve is characterized by a region where the relative length difference is constant or only slowly increasing, always less than 5%. As the cutoff cluster size s^* is reached, $\Delta l / \langle l_y \rangle$ increases significantly. Specifically, the largest sustainable clusters are roughly 30% longer in the direction of flow than transverse to the direction of flow.

To understand elongation, one has to consider how the capillary pressure at the cluster perimeter is affected by a surrounding viscous pressure field. In mechanical equilibrium, the surface pressure $P_{nw} - P_w$ equals the capillary pressure P_{cap}

$$P_{nw} - P_w = P_{\mathrm{cap}} = \gamma\left(\frac{1}{R_1} + \frac{1}{R_2}\right), \tag{12}$$

where R_1 and R_2 are the radii of curvature in the well-known *Young-Laplace* law. The wetting fluid pressure difference ΔP_w over a cluster of length l_y can be approximated as

$$\Delta P_w \approx \frac{\Delta P_{ss}}{L} l_y, \tag{13}$$

whereas the nonwetting fluid pressure P_{nw} is constant inside the cluster. The capillary pressure over the interface of the cluster will thus decrease in a direction opposite to that of the overall flow, highest at the tip and lowest at the tail of the cluster. As we shall see, this introduces anisotropy which will depend on the crossover length l^*.

In the case of steady-state simultaneous flow, the dynamics of nonwetting clusters are influenced by a competition of *both* drainage and imbibition processes. A pore is drained or imbibed when the capillary pressure is above or below the capillary threshold pressure for drainage P_c^D or imbibition P_c^I, respectively. Due to the randomness in the local geometry of the porous medium, P_c^D and P_c^I are not fixed values. As discussed by Auradou *et al.* [38], they will vary independently from pore to pore according to their respective distribution function. Furthermore, these distributions are isotropic.

Clusters of length $l_y < l^*$ are observed from experiments to migrate only small distances in the porous matrix. Usually they get trapped and can only be remobilized by coalescing with larger migrating clusters. Migration is the process where drainage is followed by imbibition, so that a cluster moves without changing its volume. The viscous pressure field sets a length scale, below which the local geometry dominates the choice of flow path. Above this length scale, growth near the advancing tip and retraction near the receding tail are favored due to the now significant capillary pressure difference between the cluster tip and tail.

As we have seen, clusters cannot grow infinitely large. It is the occurrence of snap-offs [38] of the cluster tail, caused by imbibition, that will determine the l_y extension. The probability of a cluster snap-off will mainly depend on (1) the difference between the average capillary pressure threshold for drainage and imbibition $\bar{P}_t = \bar{P}_c^D - \bar{P}_c^I$ and (2) the capillary pressure difference $\Delta P_{\text{cap}} = P_{\text{cap,tip}} - P_{\text{cap,tail}}$ [see Eq. (12)] between the advancing tip and receding tail of a cluster. Further, snap-offs will typically occur when

$$\Delta P_{\text{cap}} > \bar{P}_t. \tag{14}$$

Using Eqs. (12) and (13) we obtain the following crossover length scale from Eq. (14):

$$\frac{\Delta P_{ss}}{L} l^* = \bar{P}_t, \tag{15}$$

$$l^* = \bar{P}_t L \frac{1}{\Delta P_{ss}}. \tag{16}$$

Equation (16) predicts a cutoff length l^*, inversely proportional to ΔP_{ss}, over which clusters can stay connected. At this point an important observation is made; inserting Eq. (3) into Eq. (16), we see that the cutoff length l^* scales with the Ca number as in Eq. (11), provided $\beta = \zeta \beta_i$. All of the latter exponents have uncertainty, which within we can make the reasonable claim that they are equal, and thus that our findings are consistent with

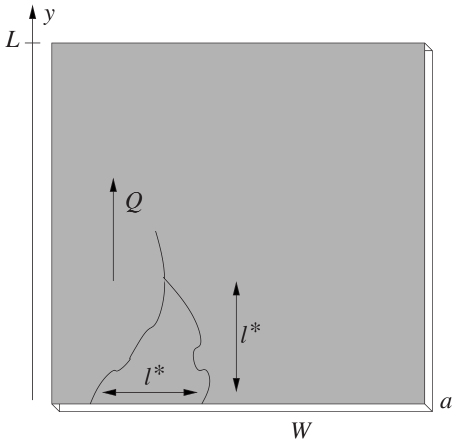

FIG. 11. A conceptual sketch of the assumed channel system. Channels of the wetting fluid, of a characteristic width that coincides with the pore width, are separated by a distance l^*. Q indicates the average direction of flow.

$$l^* \propto \frac{L}{\Delta P_{ss}}. \tag{17}$$

To sum up, we claim that Eq. (17) controls the onset of (1) cluster elongation or anisotropy as seen in Fig. 10, (2) snap-offs and the size of the largest sustainable clusters as seen in Fig. 8, and (3) cluster mobilization.

The scaling relation between ΔP_{ss} and Ca [Eq. (3)] can be derived by the following argument of dissipation balance [36]. Since the average interface area of the system will remain constant in steady state, all the power that is put into the system goes into viscous dissipation. This dissipation will then take place in the high viscous wetting fluid. The flow pattern of the wetting fluid is best described as an interchanging network in between the air clusters, containing larger islands connected by narrow channels on the order of a pore size wide. It is reasonable to assume that the majority of viscous dissipation will take place in the narrow channels, since the local flow velocity is much higher here. In this respect it is also important to remember that the permeability for the most part is set by the narrowest parts of the fastest flow path through the medium. Islands of wetting fluid do not contribute as much.

Careful visual observation indicates that the width of the channels are typically one or a few pore widths, while the spacing between these channels must be the characteristic cluster length l^*. This conceptual picture is illustrated in Fig. 11. Thus, the volume in which the dissipation happens is then assumed to be the volume of these channels and will be denoted as V_{dis}. We may then write the following proportionality for V_{dis}:

$$V_{dis} \propto \text{number of channels} = \frac{W}{l^*} \propto \Delta P_{ss}, \tag{18}$$

where the last proportionality follows from Eq. (17). On the other hand, the total work per unit time which is done by the pressure drop across the system must equal the internal dissipation D, so that

$$15Q_0\Delta P_{ss} = D \propto V_{dis}u^2, \tag{19}$$

where u is the average flow velocity of the wetting fluid and D is the integral over V_{dis} of $u|\nabla P|$. Furthermore, the pressure gradient $|\nabla P| \propto u$ thanks to Darcy's law. The flow velocity u is set by the volume flux as

$$u \propto \frac{Q_w}{V_{dis}} \propto \frac{Q_w}{\Delta P_{ss}} \tag{20}$$

by the use of Eq. (18). Upon insertion of u in Eq. (19) we may write in terms of the Ca number ($\mathrm{Ca} \propto Q_w \propto Q_0$)

$$\Delta P_{ss} \propto \sqrt{\mathrm{Ca}}, \tag{21}$$

which is the scaling relation we set out to prove. Darcy's law allows us to write things in terms of a Ca-dependent effective permeability $\kappa(\mathrm{Ca})$. Since Darcy's law takes the form

$$Q_w = \frac{\kappa}{\mu_w}\frac{\Delta P_{ss}}{L}, \tag{22}$$

we immediately obtain

$$\kappa \propto \sqrt{\mathrm{Ca}}. \tag{23}$$

We have already discussed the normalized PDF of nonwetting clusters, $p(s)$, which was shown to obey a scaling law in the cutoff cluster size s^* [Eq. (7)], and thus also in the capillary number Ca [Eq. (6)]. We now turn to a discussion of the PDF of l_i for all s, namely, the marginal PDF $p(l_i)$. Since there is no *one-to-one* correspondence between l_i and s, no exact analytical solution of $p(l_i)$ can be obtained from Eq. (5). However, $p(l_i|s)$ is Gaussian [Fig. 9(a)] and narrowly peaked around $\langle l_i \rangle$ [Eq. (10)]. On this basis we would expect $p(l_i)$ to have similarities with the PDF

$$g(l) = p(s)\frac{ds}{dl}, \tag{24}$$

$$g(l) \propto l^{-\phi}\exp\left[-\left(\frac{l}{l^*}\right)^{1/\beta_i}\right], \tag{25}$$

where

$$\phi = \frac{\tau+\beta_i-1}{\beta_i} \approx 2.9. \tag{26}$$

The function $g(l)$ is thus the PDF obtained when assuming that Eq. (9) applies for all l_i.

The PDFs $p(l_y)$ and $p(l_x)$ are plotted in Fig. 12(a), and it is evident that a cutoff behavior is dominant, similar to what is found for $p(s)$. Furthermore, for the largest extension lengths, the probability density $p(l_y)$ is larger than $p(l_x)$ for all the Ca numbers. This is intrinsically linked to the fact that large clusters are elongated in the direction of flow as discussed previously. We have already argued that there exists a cutoff length l^* common for both l_i directions. The observed difference between $p(l_x)$ and $p(l_y)$ is thus due to different cutoff behaviors in these PDFs as a consequence of elongation.

On the basis of Eq. (25) a rescaling of the form $l^{*\phi}p(l_i)$ vs l_i/l^* is predicted. The corresponding data collapse is shown in Fig. 12(b). The exponent ϕ is in this case taken as the value giving the best collapse, and it is found that $\phi = 2.8 \pm 0.3$, in agreement with Eq. (26). Again there is a crossover as the extension length approaches the pore scale, but above this scale the collapse is most satisfactory. The small difference in the cutoff function, as discussed above, is indicated by the two solid lines in Fig. 12(b). Analog to Eq. (7), $p(l_i)$ obeys the scaling function

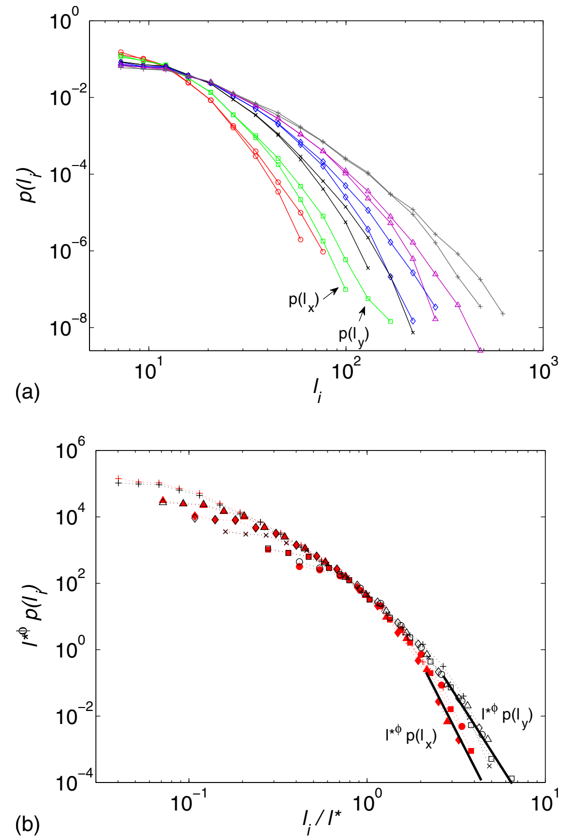

FIG. 12. (Color online) (a) Plot of the linear extension PDF $p(l_x)$ and $p(l_y)$ for various Ca numbers (similar symbol encoding as in Fig. 10). (b) shows a data collapse, predicted by Eq. (25), of the same curves. The red (dark gray) filled and black empty markers represent l_x and l_y, respectively. The exponent ϕ is taken as the value that gives the best collapse, and it is found that $\phi = 2.8 \pm 0.3$. Solid black lines indicate the difference in cutoff function of $p(l_x)$ and $p(l_y)$.

$$p(l_i) \propto l^{*-\phi}G_i(l_i/l^*), \tag{27}$$

for clusters above the lower cutoff scale.

The imposed nonwetting flow rate during steady state $Q_{nw} = 7Q_0$ must on average equal the flux of nonwetting clusters inside the model. As shown in [36], this gives a normalization condition that can be used to obtain the value of the scaling exponent ϕ, in Eq. (27),

$$Q_{nw} = \frac{aN}{L}\int_a^\infty dl\, l^2 U(l)p(l), \tag{28}$$

where we have skipped subindices. Here, N denotes the total number of clusters. Below we show that this number de-

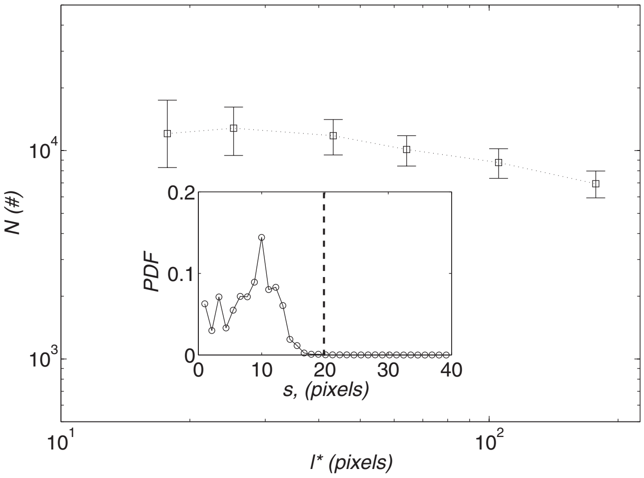

FIG. 13. Total number of clusters N in the system of area $A = L \times W$ as a function of the crossover length l^*. The upper and the lower limits of the error bars correspond to a chosen threshold of $s=14$ and $s=30$, respectively. Inset shows the size PDF of glass beads. A threshold of $s=20$ pixels ensures that no glass-bead "clusters" are included in N.

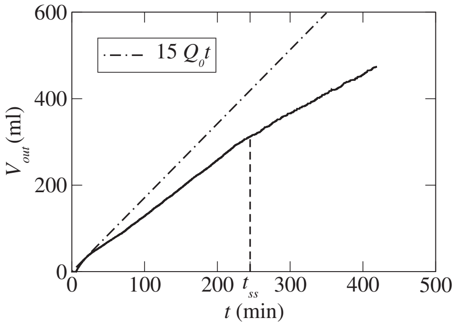

FIG. 14. The solid line is the measured accumulated outflow of the wetting phase since the start of the experiment. After the steady-state time t_{ss} the slope of this curve equals $8 \times Q_0$ as one should expect since this is the injection rate of the wetting phase. However, for $t < t_{ss}$ the pressure increases in the model, thus compressing air, and therefore the outflow of wetting fluid Q_{tot}^{inv} is less than $15 \times Q_0$ which one would expect in the case of incompressible fluids.

pends only very weakly on the flow rate. $U(l)$ denotes the average center of mass velocity of a cluster of extent l. This function is assumed to be linear in Q_{nw} and to depend only on some function $f(l/l^*)$. As a first approximation one could take $f(l/l^*) \propto \Theta(l/l^* - 1)$, where $\Theta(x)$ is the usual Lorentz-Heaviside step function, since small clusters usually are immobile,

$$U(l) = \frac{Q_{nw}}{A} f(l/l^*). \tag{29}$$

By insertion of the distribution of l_i in Eq. (27) and applying the substitution $x = l/l^*$, Eq. (28) gives

$$1 = l^{*(3-\phi)} \frac{aN}{V} \int_{a/l^*}^{\infty} x^2 f(x) G_i(x) dx, \tag{30}$$

where the integrand converges in both limits. In particular, the lower limit corresponds to immobile clusters where $U(l)=0$. If the total number of clusters N is constant with respect to l^* or Ca, we obtain immediately $\phi=3$. This is consistent with our experimental findings. We wish however to elaborate somewhat on the influence of N on the exponent ϕ, as measurements of N is found to have a weak, at most logarithmic, dependence of l^*. In counting the number of clusters, there is an experimental technicality that needs to be addressed. In the black and white images used in the cluster analysis, both the glass beads that constitute the porous medium and regions of air show up as white pixels. This means that there is a size distribution of bead "clusters" that should be disregarded from the real air cluster size distribution. Analyzing background images, i.e., images of the porous matrix filled with the black wetting fluid only, it is found that the distribution of glass beads does not exceed a size of $s=20$ pixels as shown in the inset of Fig. 13. Thus, in obtaining N we use $s=20$ pixels as a lower threshold for a cluster to be counted. However, clusters of all sizes contain pixels from both glass beads and air. As a consequence, when we are above the typical bead size, a constant size fraction is added to the original cluster size and it does not affect the analysis in any way. When clusters approach the average size of a glass bead, somewhat below the threshold, the extracted area is largely dominated by the glass bead and we have little information at this scale. This small-scale effect is most dominant in high Ca-number experiments, as air clusters are smaller here (low l^* values). In this case, the value of N will be underestimated, since there are actual air clusters smaller than the chosen glass bead threshold.

Figure 13 shows a weak decreasing trend in the number of clusters N as a function of l^*, with error bars corresponding to glass bead cluster thresholds $s=\{14,30\}$ pixels. As a matter of convenience, we quantify this dependence through a power law and we find an exponent of -0.25 ± 0.10 between N and l^*. Accounting for this dependence in Eq. (30), the exponent ϕ is reduced and we obtain $\phi=2.75$, corresponding well with the experimental value. Using this ϕ we obtain through Eq. (26) an exponent $\tau \approx 2$ for the cluster size PDF. This is also in good agreement with the found experimental value.

D. Compressibility effects

In addition to the pressure, we record the volume of wetting fluid flowing out of the model, V_{out}. This is shown in Fig. 14 for the Ca=0.032 experiment. If the fluids were incompressible, the total outflow would equal the total inflow, i.e., $15Q_0$, until the first nonwetting fluid is produced. For $t < t_{ss}$ we define the total invasion flow rate as $Q_{tot}^{inv} = dV_{out}/dt$. One observes that this slope is smaller than $15Q_0$, which is caused by air compression as the pressure increases. For each experiment this slope is found to be roughly constant, with values listed in Table II. As steady state is reached, i.e., $t \geq t_{ss}$, we expect a total flow rate of $Q_{tot} \equiv 15Q_0$. At this point the pressures are relaxed at a constant average value, and the air is not compressed any further, meaning that a flow rate of Q_0 is obtained from all seven air-filled syringes.

As an example, for Ca=0.17 the inlet and the outlet pressures during steady state are ~55 and ~5 kPa, respectively. This gives a pressure difference of ~50 kPa as seen in Fig. 4(a). This means that air entering the model has a compressed volume of roughly ~2/3 relative to the volume at the outlet. The question is to what extent air compressibility affects the flow dynamics and structure, i.e., compared to the flow of two incompressible fluids.

We claim that most of the expansion of compressed air happens during short time intervals through "avalanches" in the porous medium. In the following a qualitative description will be given. This phenomenon is a study in its own respect, and a quantitative analysis is beyond the scope of this paper. From visual inspection it is observed that air is frequently blocked out by the local configuration of wetting fluid around one or more of the air inlet nodes. This causes further compression and thereby a pressure increase in the air tubes. As the pressure continues to increase, the air is seen to slowly displace the blocking wetting fluid. At some point an avalanche of expanding air is triggered and the air and inlet pressure drop abruptly. The avalanche is characterized by channels, not more than a pore size wide, created between existing nonwetting clusters. The temporarily existing nonwetting cluster is narrow in the l_x direction but spans the air invaded region in the l_y direction. This means that an avalanche cluster reaches from the originating inlet node to either the displacement front or all the way through the model, dependent on whether the system is in the transient or in the steady state, respectively. During an avalanche in the transient state, air is seen to propagate rapidly to the displacement front where it expands surrounded only by the wetting fluid. This rapid propagation of expanding air is also seen in steady state but the air is now immediately transported to the model outlet. The time scale of an avalanche is on the order of ~1 s. During this time, a signature of the avalanche is seen as a spike in the pressure signal from the middle and the outlet pressure sensors. As the pressure inside the avalanche cluster relaxes, the interconnecting channels are imbibed by the surrounding wetting fluid and the displacement now returns to "normal." Being a highly dynamical phenomenon, the flow of expanding air in avalanches is visually striking. Figure 15 shows an avalanche through the central part of the model, also compared to normal displacement during the same time interval.

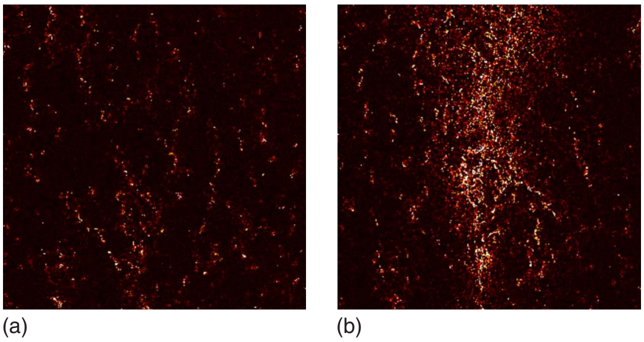

FIG. 15. (Color online) A central region of the model, (17 × 17) cm consisting of ~10^4 pores, is captured with a fast camera during steady state (Ca=0.090). Flow direction is from top to bottom. By subtracting two images of the displacement structure, separated in time by $\Delta t \sim 1$ s, pores imbibed or drained (bright regions) during this time can be distinguished from pores of unchanged fluid configuration (dark regions). (a) Normal displacement. Pore fluid configurations are close to unchanged during Δt. (b) Avalanche through the same region as depicted in (a). In this case the fluid configurations are drastically changed in a narrow central part of the image during Δt as the avalanche passes through. This is the signature of air expanding rapidly through the region.

It is not trivial to obtain the details of how the flow dynamics is affected by compressibility of the nonwetting fluid. It is clear that the avalanches occurring on small time scales are solely an effect of compressibility. However we believe that the results of our statistical analysis of clusters would be the same as in the incompressible case. Mainly there are two arguments supporting this. (1) From the above description of avalanches it is natural to assume that most of the compressed air volume inside clusters is released during an avalanche. Hence in between avalanches, the normal motion, breakup, stranding and coalescing of clusters would be as in the incompressible case. (2) Intuitively one might imagine that compressible clusters would expand and grow larger when moving toward lower pressure at the outlet, thus giving a position dependence of the cluster PDF and saturation. This is however not the case as shown in Fig. 16, where the distribution of clusters from two different regions of the model are compared and found to be identical. Thus, the saturation and the distribution of clusters are homogeneous throughout the model, as expected for an incompressible system. This can be explained by recalling the importance of the viscous pressure drop in the wetting fluid, which in essence determines the size of nonwetting clusters through the cutoff length or size, as argued previously. Either if clusters expand due to compressibility or, e.g., because two smaller clusters coalesce to make one big cluster, snap-off will occur at the cutoff size regardless of the origin of growth.

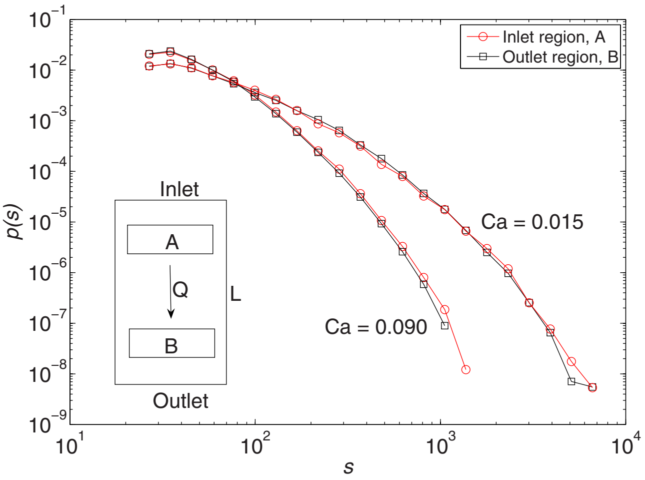

FIG. 16. (Color online) Cluster size PDF $p(s)$, for Ca=0.090 and Ca=0.015. For each Ca number a region A close to the inlet and region B close to the outlet has been considered, as shown in the inset sketch. It is evident that the clusters are distributed equally in the direction of flow and not affected by air compressibility. This behavior is found to apply for all Ca numbers considered in the experiments.

IV. CONCLUSION

Simultaneous two-phase flow in porous media has been studied experimentally, in a large quasi-two-dimensional laboratory model of roughly $\sim 10^5$ pores. We use a gas-liquid phase pair, resulting in a low viscosity ratio $M \sim 10^{-4}$. Both the transient and the steady states of this system have been considered.

The mixed displacement structure of wetting and nonwetting fluids is more complex than what is found in the transient regimes of, e.g., capillary or viscous fingering. Due to the simultaneous flow of high viscous wetting fluid, clusters of low viscous nonwetting fluid will be snapped off from the inlet nodes. The competition of both drainage and imbibition causes fragmentation of the nonwetting fluid, and the dynamics is characterized by the movement and mixing of discreet nonwetting clusters in a background field of wetting fluid. Initially, the fragmentation and the mixing of fluids increase, but are seen to stabilize when the most advanced parts of the front have reached roughly halfway through the model. At this point the invasion structure consists of a heterogeneous region at the front and a homogeneous region further behind, locally in steady state, similar to that of later global steady state. It is an important result, because this kind of similarity between transient and steady regimes is far from obvious.

The probability distribution of the size of nonwetting clusters exhibits a clear cutoff for all Ca numbers investigated during steady state. No clear power-law behavior is found, however, for larger clusters reasonable fits are obtained to Eq. (5). We find $\tau \approx 2$ and that the cutoff cluster size s^* is inversely proportional to the capillary number. Additionally a scaling relation is found between the mean extension length $\langle l_i \rangle$ and $s \leq s^*$, equal in both directions with the exponent $\beta_i \approx 0.57$. Clusters at these sizes are thus isotropic. Clusters above s^* are elongated in the direction of flow due to the anisotropic influence of the viscous pressure field. From these scaling relations we demonstrate experimentally and theoretically the important result that both $1/l^*$ and ΔP_{ss} scale approximately as the square root of the Ca number.

The observed avalanche behavior, occurring in the compressible nonwetting phase, is an interesting phenomenon that we have not explored fully in this work. To the best of our knowledge, this kind of dynamics in a gas-liquid system in porous media has not previously been reported. To characterize and obtain a better understanding of these dynamical events is certainly something worthy to pursue.

In a recent paper by Ramstad and Hansen [35], cluster size distributions during steady-state two-phase flow in a porous medium was studied numerically for $M=1$, i.e., viscosity match of the fluid pair. They found that below a critical value of the nonwetting fluid saturation, the nonwetting cluster size distribution was dominated by a cutoff behavior similar to what have been presented here. Above the critical saturation value, power-law behavior was observed. Due to the large difference in viscosity contrast between our experiments and these simulations, no direct comparison can be made. Nevertheless, it would be interesting to perform future experiments with the intention of exploring such a critical value.

Despite the variety of findings in this study, only a small part of the parameter space was explored. Our theoretical predictions should be used as a starting point of incorporating the more complex case of, e.g., viscosity matched fluids. Thus, we would like in the future to consider experiments where the two phases has more similar viscosities and also the possibility of tuning the wetting and the nonwetting fluid flow rates independently. At the present time, preliminary results indicate that the flow dynamics show no strong dependence of the latter flow parameter. Finally, the question of any history dependence of the global steady state is important. It is not obvious that the system will reorganize itself to a unique steady-state structure independent on initial transients. However, a preliminary steady-state experiment, initially at Ca=0.0027 and then increased to Ca=0.032, shows that the structure organizes into a statistically identical structure as in an ordinary Ca=0.032 experiment.

ACKNOWLEDGMENTS

The work was supported by The Norwegian Research Council through PETROMAKS. We thank Olav Aursjø, Renaud Toussaint, and Alex Hansen for useful comments.

---

[1] J. Bear, *Dynamics of Fluids in Porous Media* (American Elsevier Publishing Company, New York, 1972).

[2] F. A. L. Dullien, *Porous Media Fluid Transport and Pore Structure*, 2nd ed. (Academic Press, Inc., San Diego, 1992).

[3] M. Sahimi, *Flow and Transport in Porous Media and Fractured Rock* (VCH Verlagsgesellschaft mbH, Weinheim, 1995).

[4] M. Sahimi, Rev. Mod. Phys. **65**, 1393 (1993).

[5] R. Lenormand, E. Touboul, and C. Zarcone, J. Fluid Mech. **189**, 165 (1988).

[6] R. Lenormand and C. Zarcone, Transp. Porous Media **4**, 599 (1989).

[7] P. G. Saffman and G. Taylor, Proc. R. Soc. London, Ser. A **245**, 312 (1958).

[8] R. Lenormand, C. Zarcone, and A. Sarr, J. Fluid Mech. **135**, 337 (1983).

[9] R. Lenormand, J. Phys.: Condens. Matter **2**, SA79 (1990).

[10] R. Lenormand and C. Zarcone, Phys. Rev. Lett. **54**, 2226 (1985).

[11] D. Wilkinson and J. F. Willemsen, J. Phys. A **16**, 3365 (1983).

[12] L. Paterson, Phys. Rev. Lett. **52**, 1621 (1984).

[13] K. J. Måløy, J. Feder, and T. Jøssang, Phys. Rev. Lett. **55**, 2688 (1985).

[14] J. P. Stokes, D. A. Weitz, J. P. Gollub, A. Dougherty, M. O. Robbins, P. M. Chaikin, and H. M. Lindsay, Phys. Rev. Lett. **57**, 1718 (1986).

[15] D. A. Weitz, J. P. Stokes, R. C. Ball, and A. P. Kushnick, Phys.

Rev. Lett. **59**, 2967 (1987).

[16] Grunde Løvoll, Yves Meheust, Renaud Toussaint, Jean Schmittbuhl, and Knut Jorgen Måløy, Phys. Rev. E **70**, 026301 (2004).

[17] O. I. Frette, K. J. Måløy, J. Schmittbuhl, and A. Hansen, Phys. Rev. E **55**, 2969 (1997).

[18] Y. Meheust, G. Løvoll, K. J. Måløy, and J. Schmittbuhl, Phys. Rev. E **66**, 051603 (2002).

[19] C. D. Tsakiroglou, M. A. Theodoropoulou, and V. Karoutsos, AIChE J. **49**, 2472 (2003).

[20] C. D. Tsakiroglou, M. A. Theodoropoulou, V. Karoutsos, D. Papanicolaou, and V. Sygouni, J. Colloid Interface Sci. **267**, 217 (2003).

[21] C. D. Tsakiroglou, M. A. Theodoropoulou, V. Karoutsos, and D. Papanicolaou, Water Resour. Res. **41**, W02014 (2005).

[22] M. A. Theodoropoulou, V. Sygouni, V. Karoutsos, and C. D. Tsakiroglou, Int. J. Multiphase Flow **31**, 1155 (2005).

[23] D. G. Avraam and A. C. Payatakes, J. Fluid Mech. **293**, 207 (1995).

[24] D. G. Avraam and A. C. Payatakes, Transp. Porous Media **20**, 135 (1995).

[25] C. D. Tsakiroglou, D. G. Avraam, and A. C. Payatakes, Adv. Water Resour. **30**, 1981 (2007).

[26] G. N. Constantinides and A. C. Payatakes, J. Colloid Interface Sci. **141**, 486 (1991).

[27] G. N. Constantinides and A. C. Payatakes, AIChE J. **42**, 369 (1996).

[28] M. S. Valavanides, G. N. Constantinides, and A. C. Payatakes, Transp. Porous Media **30**, 267 (1998).

[29] D. G. Avraam and A. C. Payatakes, Ind. Eng. Chem. Res. **38**, 778 (1999).

[30] M. S. Valavanides and A. C. Payatakes, Adv. Water Resour. **24**, 385 (2001).

[31] A. Vedvik, G. Wagner, U. Oxaal, J. Feder, P. Meakin, and T. Jøssang, Phys. Rev. Lett. **80**, 3065 (1998).

[32] H. A. Knudsen, E. Aker, and A. Hansen, Transp. Porous Media **47**, 99 (2002).

[33] H. A. Knudsen and A. Hansen, Phys. Rev. E **65**, 056310 (2002).

[34] H. A. Knudsen and A. Hansen, EPL **65**, 200 (2004).

[35] T. Ramstad and A. Hansen, Phys. Rev. E **73**, 026306 (2006).

[36] A. C. Payatakes, Annu. Rev. Fluid Mech. **14**, 365 (1982).

[37] D. Stauffer and A. Aharony, *Introduction to Percolation Theory* (Taylor & Francis, London, 1992).

[38] H. Auradou, K. J. Måløy, J. Schmittbuhl, and A. Hansen, Transp. Porous Media **50**, 267 (2003).

[39] K. T. Tallakstad, H. A. Knudsen, T. Ramstad, G. Løvoll, K. J. Måløy, R. Toussaint, and E. G. Flekkøy, Phys. Rev. Lett. **102**, 074502 (2009).